Study of the Layered Magnetoresistive Perovskite $La_{1.2}Sr_{1.8}Mn_2O_7$ by High-Resolution Electron Microscopy and Synchrotron X-ray Powder Diffraction

R. Seshadri, M. Hervieu, C. Martin, A. Maignan, B. Domenges, and B. Raveau*

Laboratoire Crismat, CNRS URA 1318, ISMRA et Université de Caen, Bd. du Maréchal Juin, 14050 Caen Cedex, France

A. N. Fitch

European Synchrotron Radiation Facility, BP 220, 38043 Grenoble Cedex, France

Received November 19, 1996. Revised Manuscript Received March 18, 1997[⊗]

The layered manganite $La_{1.2}Sr_{1.8}Mn_2O_7$ is important in that it displays giant negative magnetoresistance properties, and its study complements the growing body of what we know about the complex size−charge−temperature−magnetic field parameter space of the perovskites $A^{III}_{1-x}A'^{II}_xMnO_3$. We report here the results of a detailed characterization of the microstructure and structure of this layered phase by high-resolution electron microscopy and synchrotron X-ray powder diffraction (SXPD). The high resolution of the data has permitted the quantification of stacking faults. The SXPD data have also been treated using Rietveld analysis. We reexamine the magnetic and transport properties of this phase. The study highlights the importance of the two-dimensional (2D) nature of the title phase.

Introduction

The layered manganite $La_{1.2}Sr_{1.8}Mn_2O_7$[1,2] crystallizes in the structure of the $m = 2$ member of the Ruddlesden−Popper series, $SrO[SrTiO_3]_m$.[3] Interest in this manganite arises from the observation that when it is cooled below 130 K it undergoes a transition to a ferromagnetic state, accompanied by a change in the temperature coefficient of resistivity from negative and insulating, to positive and metal-like. In this, the behavior parallels that of the related perovskites $A^{III}_{1-x}A'^{II}_xMnO_3$.[4−6] Recent investigations have demonstrated that near and below the transition to a ferromagnetic state, the application of a magnetic field induces a large decrease of the resistivity in these layered phases, *i.e.*, they display giant negative magnetoresistance.[7−9] While the observed magnetoresistance ratios $\rho(0)/\rho(H)$ are much smaller in these phases than values found in certain perovskites,[10−13] they are interesting nonetheless in that they add to our understanding of the complex magnetostructural phenomena and magnetotransport in these manganites.

High-resolution electron microscopy has permitted a detailed microstructural characterization, which we present here. In a layered material such as the title phase, stacking faults are ubiquitous and could considerably influence the properties; this underlines the importance of such a study. Using clues from microscopy as to the nature of the defect structure, we have exploited the high resolution of the SXPD patterns to quantify the occurrence of adventitious intergrowth defects, by comparing the experimental SXPD profiles with profiles simulated from the stacking of certain structural motifs.

In two previous publications, we presented detailed studies of the evolution of structure and magnetotransport as RE size is changed in the phases $RE_{1.2}Sr_{1.8}Mn_2O_7$,[9] and as Mn^{IV} content is varied in the phases $La_{1+x}Sr_{2-x}Mn_2O_7$.[14] In both cases, we found that an interesting feature of these *I*4/*mmm* phases is the possibility of tuning the way in which the rare-earth and Sr cations distribute between the two sites permitted them in this structure; the one, a 12-coordinate site within the double perovskite layer, labeled P, and the other, a nine-coordinate site in the rock-salt part of the structure, labeled R. Figure 1 shows a schematic representation of this structure. Our structural investigations of these phases involved the Rietveld analysis of laboratory powder X-ray data, with the associated problems of limited instrumental resolution as well as a limited range in $q = \sin(\theta)/\lambda$. Specifically, while RE and Sr are sufficiently contrasted in an X-ray diffraction experiment, the determination of the distribution of RE and Sr between the two sites was correlated with the

[⊗] Abstract published in *Advance ACS Abstracts,* July 1, 1997.

(1) MacChesney, J. F.; Potter, J. F.; Sherwood, R. C. *J. Appl. Phys.* **1969**, *40*, 1243.
(2) Mohan Ram, R. A.; Ganguly, P.; Rao, C. N. R. *J. Solid State Chem.* **1987**, *70*, 82.
(3) Ruddlesden, S. N.; Popper, P. *Acta. Crystallogr.* **1958**, *11*, 54.
(4) Jonker, G. H.; van Santen, J. H. *Physica* **1950**, *16*, 337.
(5) Zener, C. *Phys. Rev.* **1951**, *82*, 403.
(6) deGennes, P. G. *Phys. Rev.* **1960**, *118*, 141.
(7) Moritomo, Y.; Asamitsu, A.; Kuwahara, H.; Tokura, Y. *Nature* **1996**, *380*, 141.
(8) Mahesh, R.; Mahendiran, R.; Raychaudhuri, A. K.; Rao, C. N. R. *J. Solid State Chem.* **1996**, *122*, 448.
(9) Seshadri, R.; Martin, C.; Maignan, A.; Hervieu, M.; Raveau, B.; Rao, C. N. R. *J. Mater. Chem.* **1996**, *6*, 1585.
(10) Kusters, R. M.; Singleton, J.; Keen, D. A.; McGreevy, R.; Hayes, R. *Physica B* **1989**, *155*, 362.
(11) von Helmholt, R.; Wecker, J.; Holzapfel, B.; Schultz, L.; Samwer, K. *Phys. Rev. Lett.* **1993**, *71*, 2331.
(12) Maignan, A.; Simon, Ch.; Caignaert, V.; Raveau, B. *Solid State Commun.* **1995**, *96*, 623.
(13) Yoshizawa, H.; Kawano, H.; Tomioka, Y.; Tokura, Y. *J. Phys. Soc. Jpn.* **1996**, *65*, 1043.
(14) Seshadri, R.; Martin, C.; Hervieu, M.; Raveau, B.; Rao, C. N. R. *Chem. Mater.* **1997**, *9*, 270.

S0897-4756(96)00593-5 CCC: $14.00

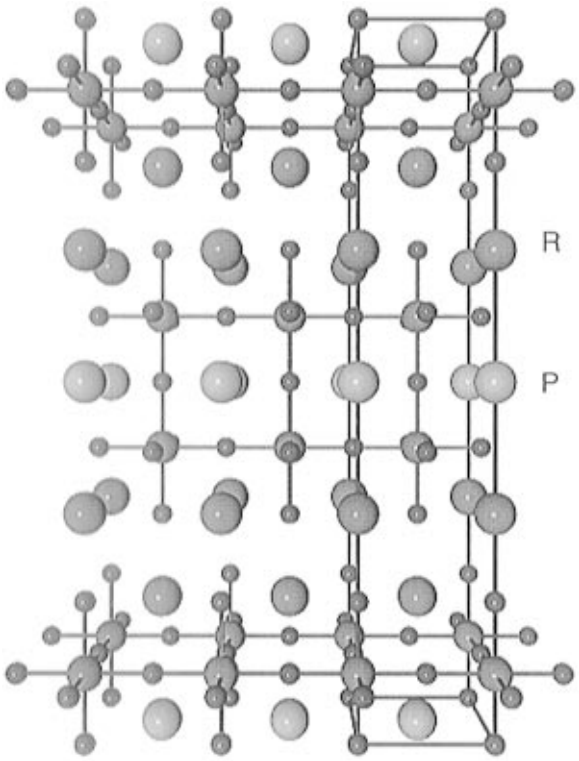

Figure 1. Structure of the title phase. The P and R sites, both occupied by (La,Sr) are labeled.

thermal parameters and the refinement of the former precluded obtaining sensible thermal parameters. We thought it thus essential to acquire high-resolution powder X-ray data over a larger dynamic range at a synchrotron source and to this end, we have collected such data on a sample of $La_{1.2}Sr_{1.8}Mn_2O_7$ at the high-resolution powder diffraction beamline BM-16 at the European Synchrotron Radiation Facility. To increase the reliability in the determination of the La and Sr distributions between the P and R sites of the structure, we have collected the data sets at three wavelengths near the La K edge and one far from the edge.[15] The Rietveld refinement and the defect structure simulation complement each other and together provide a complete analysis of the SXPD data.

The magnetic properties, focusing on elevated temperatures, have also been reexamined and the results which include a magnetic anomaly around 500 K not previously marked are presented here. The interpretation of the properties is strengthened by a detailed knowledge of the microstructure and are thus found to be intrinsic to the title formulation.

While the results presented here describe the structure and properties of a single sample, we believe the conclusions drawn are of some general interest; to GMR manganites as well as to a large class of layered materials with interesting electronic properties.

Experimental Section

The sample preparation has been detailed in earlier publications[9,14] and included the crucial addition of a small amount of Bi_2O_3 in excess of the stoichiometry. Oxygen content was verified to correspond to the title stoichiometry, $O_{7.00(2)}$, by titration against the Fe^{III}/Fe^{II} couple using a redox indicator.

Samples for electron microscopy combined with energy-dispersive X-ray analysis (EDS) were prepared by crushing a powder in alcohol and dispersing the small flakes on a carbon grid. Numerous crystallites were characterized using electron diffraction (ED) and high-resolution electron microscopy (HREM). Reconstruction of the reciprocal space was possible using ED patterns acquired on a JEOL 200CX microscope fitted with a tilting−rotating sample holder capable of orienting through ±30°. The HREM study was performed on a TOPCON 002B electron microscope capable of a point-to-point resolution of 1.8 Å. Both microscopes are equipped with Kevex EDS analyzers.

X-ray diffraction data on powders was acquired with the sample in a borosilicate glass capillary of 0.3 mm diameter using the nine-channel multianalyzer stage (Ge(111)) at the newly installed high-resolution powder diffractometer on Beamline BM-16 of the European Synchrotron Radiation Facility.[16] The nine detectors (separated by 2°) are scanned continuously through the desired range in 2θ with the data being collected while monitoring the 2θ positions of the detectors using a highly accurate encoder. The line width was clearly defined by the sample rather than the diffractometer and suggested a suitable rebinning of the collected data in steps of 0.005° in 2θ. All data were collected at wavelengths close to or smaller than 0.4 Å, resulting in negligible sample absorption. To determine the wavelengths for acquiring anomalous scattering data, the X-ray fluorescence yield from the sample was measured using a scintillation counter held at approximately 90° to the sample with respect to the beam, while scanning the monochromator angle.

Magnetic studies were performed using a Quantum Design MPMS SQUID magnetometer and a home-built Faraday balance. Magnetotransport studies were carried out on a Quantum Design physical property measurement system on sintered bars of the sample to which copper leads were ultrasonically attached using indium solder.

Results and Discussion

Electron Microscopy. From the reconstruction of the reciprocal space performed on numerous crystallites, the homogeneity of the sample was confirmed, with no impurity being detected. The cell symmetry was seen to be tetragonal with $a \sim a_P$ (the ideal cubic perovskite cell), and $c \sim 20$ Å as expected for the $m = 2$ Ruddlesden−Popper phase. The observation of reflections with the limiting conditions hkl; $h + k + l = 2n$ were in agreement with the I centering of the unit cell. [001] and [010] ED patterns are displayed in Figure 2. Parts of certain crystallites exhibited diffuse streaks along c^*, suggesting stacking defects. The characterization of these defects was made using HREM. These defective portions of crystals also displayed variations in the stoichiometry from the nominal cation stoichiometry $La_{1.2}Sr_{1.8}Mn_2$ otherwise established by EDS in the majority of the grains. We return to these defect features shortly.

Crystals exhibiting ED patterns similar to those displayed in Figure 2 were characterized by a nearly perfect matrix with very few intergrowth or other defects. One typical overall image of the (010) planes is shown in Figure 3a. The fringe periodicity is ~10 Å corresponding to $c/2$. A very regular distribution of the fringes is observed, which attests to the high degree of perfection of the particular crystal. The crystallinity in this example is however interrupted by three defective members indicated by black triangles. In an enlarged portion of this [010] image shown in Figure 3b, the layer

(15) The anomalous contribution to the scattering at and near the La K edge is negative, so it actually *decreases* the contrast between La and Sr. Our aim in acquiring these data has been in increasing the redundancy in the data with respect to the number of refined parameters.

(16) Fitch, A. N. *Mater. Sci. Forum* **1996**, *228−231*, 219.

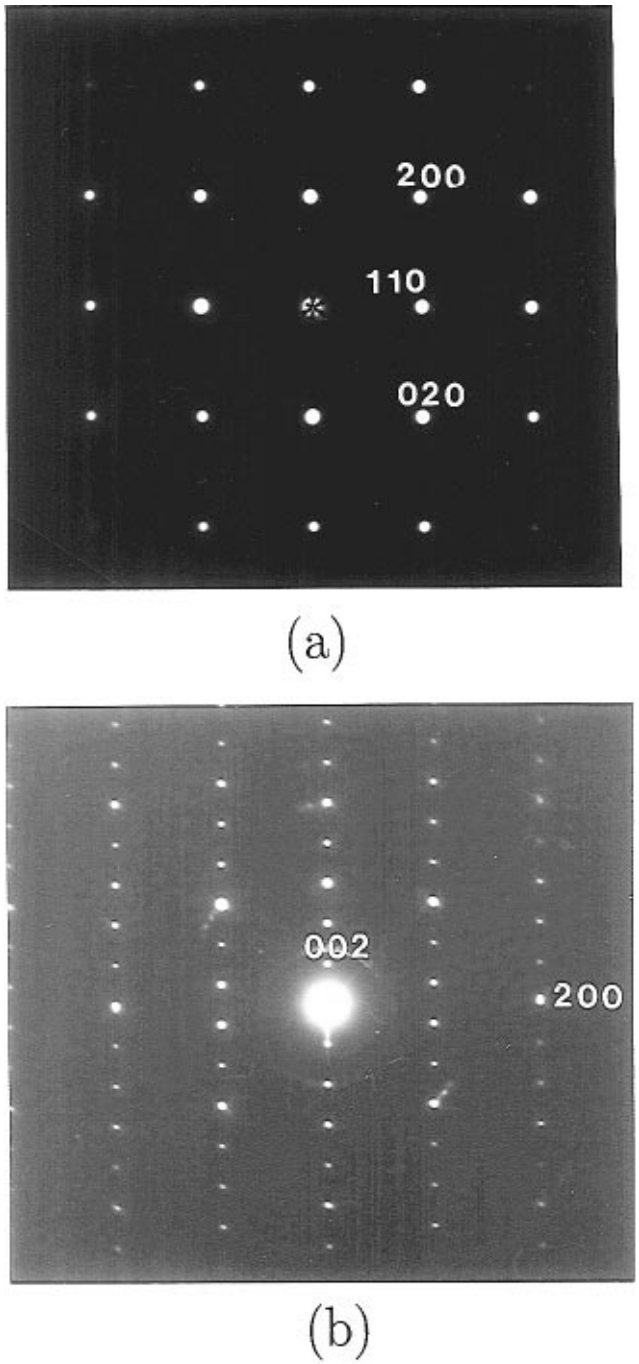

Figure 2. (a) [001] ED patterns of the title phase showing the $a_P \times a_P$ periodicity in the basal plane. (b) [010] ED pattern showing reflections due to 00*l* planes.

stacking along $\vec{c}$ is clearly seen to involve two rows of staggered, dark dots corresponding to the cations in the R site, with the rows separated by ~2.6 Å. This is the rock-salt slab of the $m = 2$ structure. Between these double rows, the familiar contrast of the perovskite structure is observed, with two rows of gray dots corresponding to the positions of Mn, separated by a single row of dark dots corresponding to the P site in the structure, which has (La, Sr) in 12-coordination. The HREM image in Figure 3b in effect provides the same view of the structure as Figure 1. Superimposed on Figure 3b is the simulated image (using the multislice method implemented in the MACTEMPAS software) for a crystal with a thickness of 15 Å and for a focus value close to −200 Å. The positional parameters used for the simulation were obtained from the refinement of the powder X-ray data as discussed in the next subsection.

The nature and the distribution of the defects which generate the streaks along *c** were studied in detail, chosing [010] and [110] images. While in general the crystals showed very few defects, we could, in certain cases, find high defect densities, sometimes within the same crystal. Figure 4a is a typical example of one such crystal, with the (110) planes being viewed. In the part of this crystal labeled **A** the fringes are regularly spaced at 10 Å intervals corresponding to the perfect $m = 2$ structure. Very few streaks are observed along *c** in the SAED pattern taken from such a domain as shown in Figure 4b. In another part of the same crystal labeled **B** there appear to be numerous stacking defects. The corresponding SAED pattern shown in Figure 4c shows considerable streaking along *c**.

The defective region in Figure 4a has been magnified and displayed in Figure 5. To facilitate the interpretation of the HREM image in Figure 5, a focus value close to −600 Å was chosen so that cation positions are imaged as bright dots. Thus the contrast of the normal $m = 2$ structure between the 10 Å fringes consists of one double row and one single row of bright spots corresponding respectively to the R and P sites occupied by (La,Sr). These are separated by a row of gray dots corresponding to the Mn positions. The simulation of a part of the image is shown as an inset in Figure 5, with the A cations (La and Sr) as well as the Mn positions labeled. The nature of the stacking faults seen in Figure 5 is now clear: It corresponds to other intergrowth members in the series $[(La,Sr)O][(La,Sr)MnO_3]_m$. We see that $m = \infty$ would correspond to the perovskite $(La,Sr)MnO_3$, $m = 1$ to the K_2NiF_4 related oxide $(La,Sr)_2MnO_4$ and so on. To identify the different values of *m*, we note that each isolated row of single dots corresponding to the *P* site is counted as $m - 1$. In the example shown in Figure 5, *m* is seen to range from 2 to 4. These *m* values have been indicated at the bottom of Figure 5.

Laffez et al.[17] have recently reported detailed microscopy studies of the $m = 2$ manganites in the system $(Pr,Nd,Ba,Ca)_3Mn_2O_7$. They observed, along with defects similar to those presented in this study, an orthorhombic distortion accompanied by a doubling of the basal plane, with $a \sim b \sim a_P\sqrt{2}$. Interestingly, while the bulk of the crystallites in the present study are I-centered tetragonal with $a \sim a_P$, in the lattice images and SAED patterns corresponding to defective regions we observe evidence for $a_P\sqrt{2} \times a_P\sqrt{2}$ periodicity, particularly for defects with large *m* members. This is clearly seen in Figure 6, where we have managed to find a region corresponding to an $m = 11$ defect member. A periodicity of 5.6 Å corresponding to $\sim a_P\sqrt{2}$ is clearly seen within the perovskite slice. Moreover, the centered contrast in this defective slice involves a local periodicity of $2a_p$ along $\vec{c}$, suggesting that this slice behaves as a perovskite inclusion or domain, rather than a true $m =$ 11 member; the nature of the distortion being unique to the domain. We know from the literature that a perovskite with the same La:Sr ratio of 0.4:0.6 as the title formulation, corresponds, assuming no oxygen defects, to a rhombohedrally distorted perovskite.[18]

In the discussion of the HREM image shown in Figure 3a, we mentioned that the regularity of the crystal is

(17) Laffez, P.; van Tendeloo, G.; Seshadri, R.; Hervieu, M.; Martin, C.; Maignan, A.; Raveau, B. *J. Appl. Phys.* **1996,** *80,* 5850.

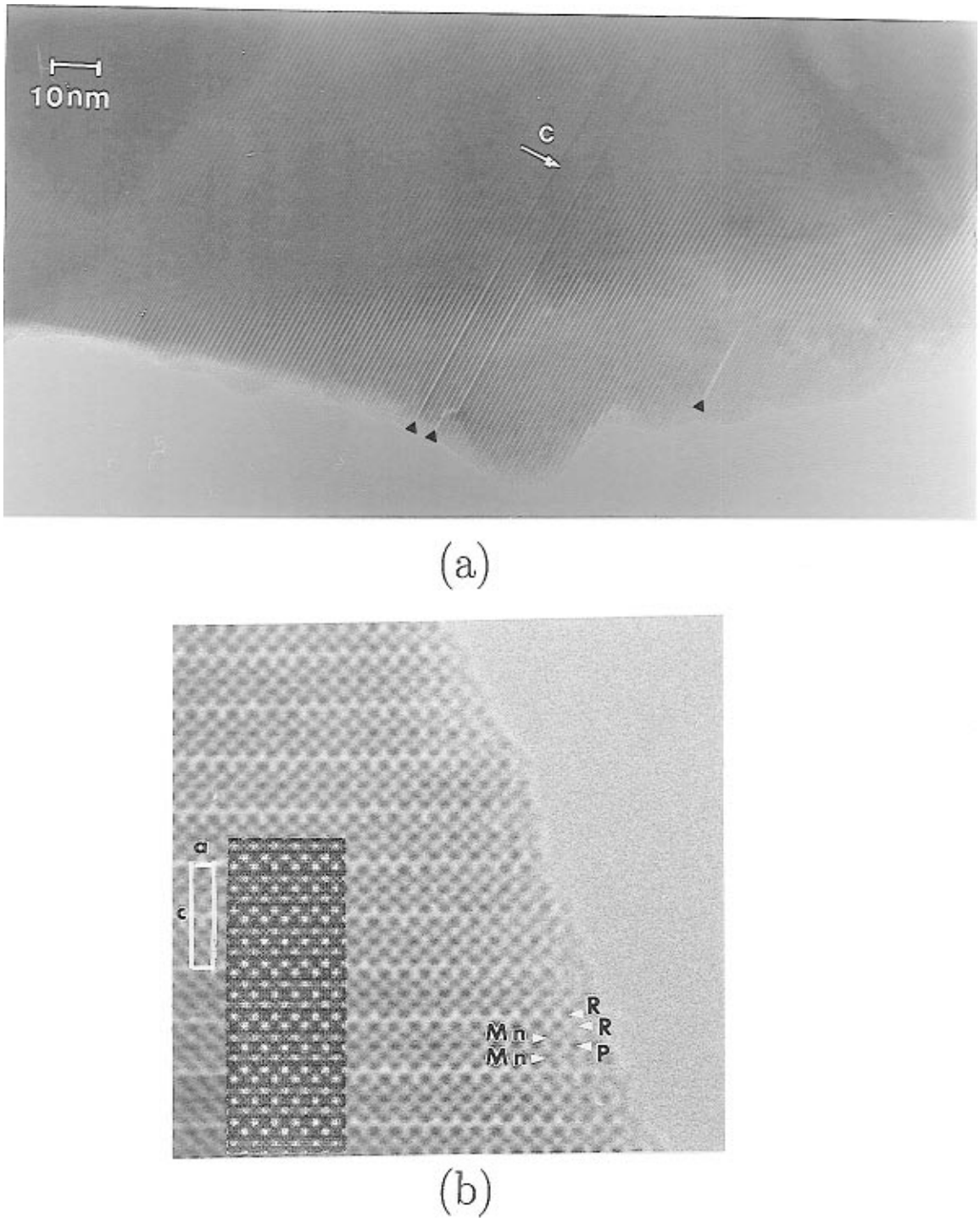

Figure 3. (a) Overall [010] image of the title phase, bearing witness to the high crystallinity. The black triangles mark defects that interrupt the *ab* crystallinity. (b) High-resolution [010] image of the title phase. The inset is a simulated image. A unit cell is also shown, and the cation positions are marked.

interrupted by three defects marked by arrows. These are of interest since they correspond to an interruption of crystallinity in the *ab* plane as opposed to an intergrowth defect which would interrupt crystallinity along $\vec{c}$. This kind of defect (which is indeed rare in the present case) arises from a local shear along $\vec{c}$ and involves the mixing of rock-salt and perovskite motifs within a layer. As a consequence of such dislocation, a distortion of adjacent layers is observed, which serves to compensate for the defect. A schematic drawing of how this can be achieved is displayed in Figure 7.

Quantifying the Defect Structure. The HREM images suggest that the defects correspond preponderantly to other intergrowth members, in other words, to stacking faults. Encouraged by the high resolution of the SXPD data, we have attempted to obtain quantitative estimates of the probability of adventitious intergrowths corresponding to these higher members. For this, we have made use of the DIFFAX program, which simulates diffraction patterns from real-space models of stacking.[19] The structure was simulated by stacking two different kinds of layers according to specific stacking sequences. The two layers used comprised (La, $Sr)_3Mn_2O_7$ units (layer **1**) and (La,Sr)MnO_3 units (layer

(18) Moritomo, Y.; Asamitsu, A.; Tokura, Y. *Phys. Rev. B* **1995,** *51,* 16491.

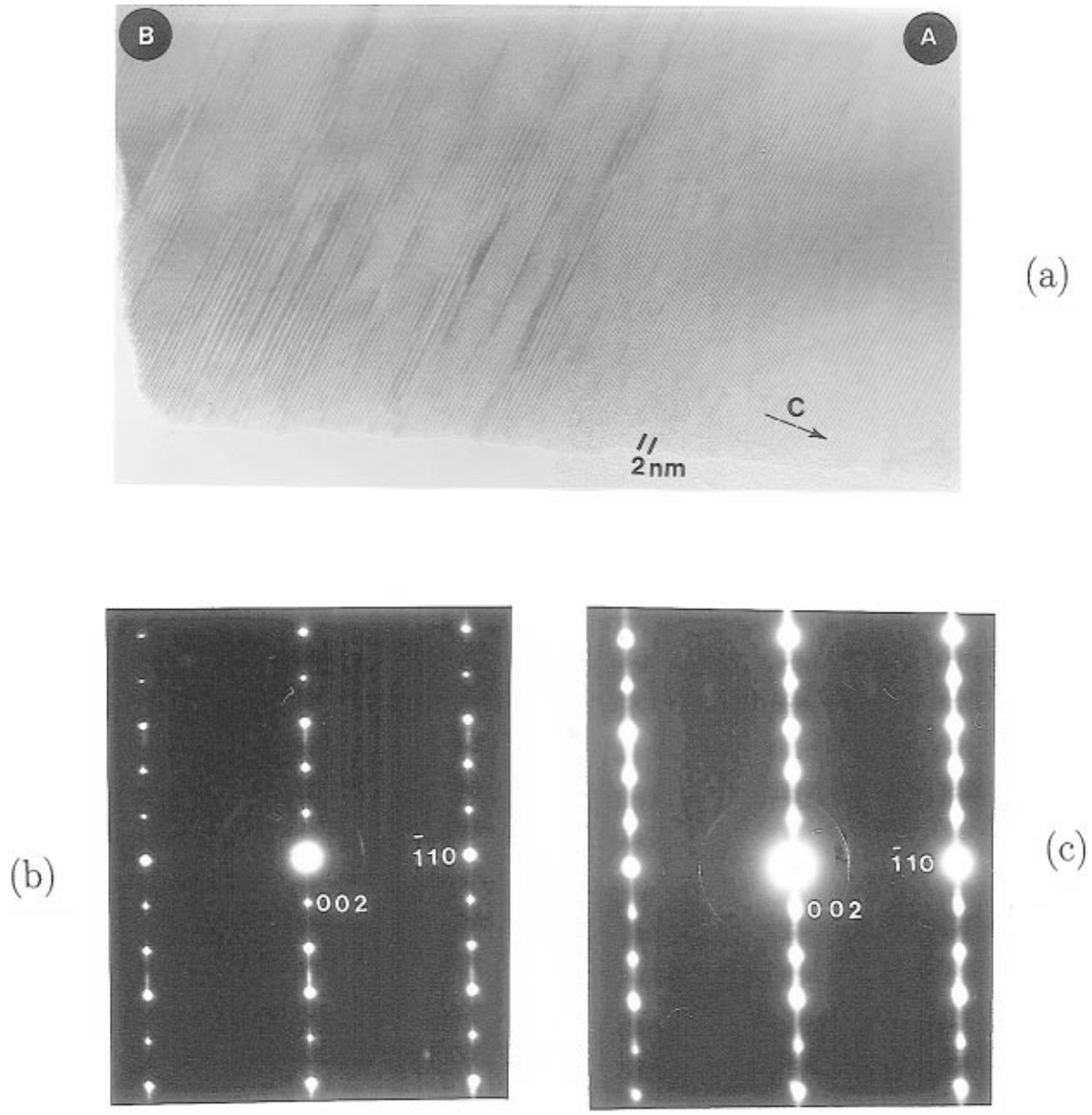

Figure 4. (a) [110] image of a crystal showing a fault-free portion (**A**) and a highly faulted portion (**B**). (b) SAED pattern obtained from the portion of the crystal marked **A** in panel (a) of this figure. Note the sharp 00*l* reflections. (c) SAED pattern obtained from the faulted portion of the crystal marked **B** showing streaking along *c**.

2). These units are depicted in Figure 8, as are the different stacking possibilities. The corresponding parameters used were $a = 3.874$ Å, $c_1 = 10.0595$ Å, and $c_2 = 3.670$ Å, suggested from the Rietveld refinement described in the next section. The vectors used for the stacking were

1 on **1**: $\vec{r} = \{x,y,z\} = \{0.5,0.5,1.0\}$

2 on **1**: $\vec{r} = \{x,y,z\} = \{0.5,0.5,1.0\}$

1 on **2**: $\vec{r} = \{x,y,z\} = \{0.0,0.0,0.3648\}$

2 on **2**: $\vec{r} = \{x,y,z\} = \{0.0,0.0,0.3648\}$

where *x*,*y*,*z* are the components of the stacking vector scaled by the lattice parameters of the cell corresponding to layer **1**. The simulated patterns were broadened using a pseudo-Voigt profile with widths and their dependence on scattering angle defined by the traditional *U*,*V*,*W* parameters. An additional parameter η defined the mixing of Lorentzian and Gaussian contributions to the line shape. These parameters were obtained from Rietveld refinement of the SXPD data using the program FULLPROF[20] and corresponded to $U = 0.708$, $V = -0.110$, $W = 0.0071$, and $\eta = 0.6$. The simulations were compared with the off-edge data acquired at a wavelength of 0.401 09 Å. The symmetry and composition that ensued from such stacking were output by the DIFFAX program and served as a check on the validity of the model, as did the patterns simulated by using **1** on **1** stacking (the defect-free $m = 2$ member) and **2** on **1** stacking (the defect-free $m = 3$ member).

(19) (a) Treacy, M. M. J.; Deem, M. W.; Newsam, J. M., computer program DIFFAX version 1.79, 1990. (b) Treacy, M. M. J.; Newsam, J. M.; Deem, M. W. *Proc. R. Soc. London A* **1991,** *433*, 499. (c) Treacy, M. M. J.; Newsam, J. M.; Deem, M. W. *Ultramicroscopy* **1993**, *52*, 512.

(20) Rodriguez-Carvajal, J. In *Proc. Satellite Meeting on Powder Diffraction of the XV Congress of the IUCr.*; Toulouse, France 1990.

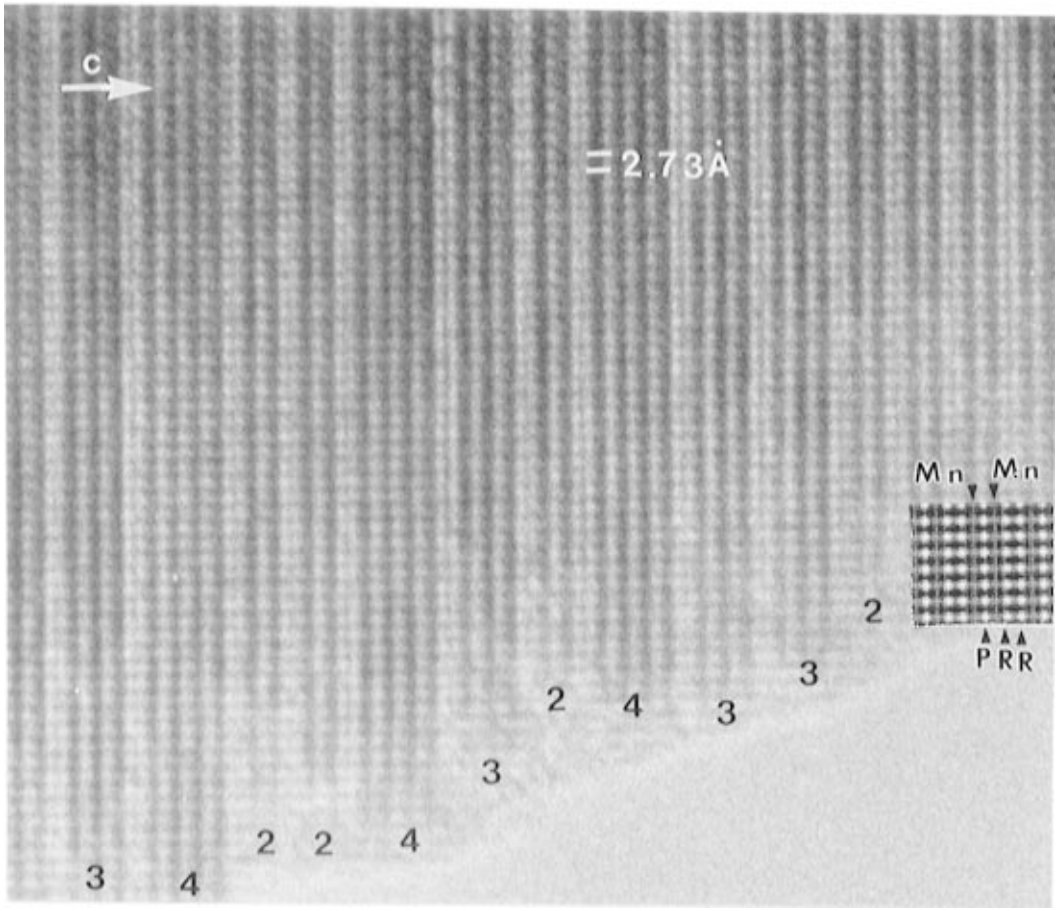

Figure 5. Defective region in Figure 4a magnified and labeled. The nature of the intergrowth defects are clearly seen to correspond to other members of the Ruddlesden−Popper series whose sizes are indicated by the numbers.

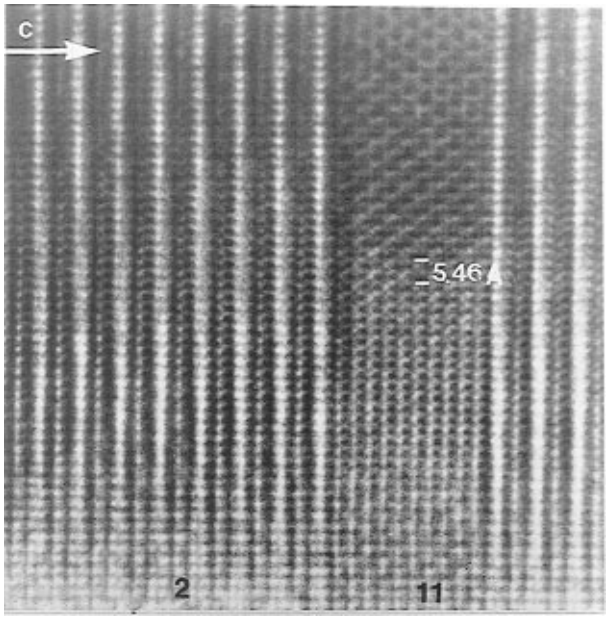

Figure 6. (a) [110] HREM image of a portion of a crystal displaying a defect $m = 11$ intergrowth member.

For the defect simulation, the stacking sequences were input explicitly as strings of digits of the form (for example) 111212..., where the digits correspond to the layer type. These strings were generated using either pseudo-random numbers (Monte Carlo) or in a quasi-random manner using the Sobol′ sequence, with a probability p for the insertion of layer **2**. The Sobol′ sequence fills space in a maximally avoiding manner.[21] We were motivated in using such a sequence by the possibility that intergrowth defects could display staging as seen in intercalated graphite for example.[22]

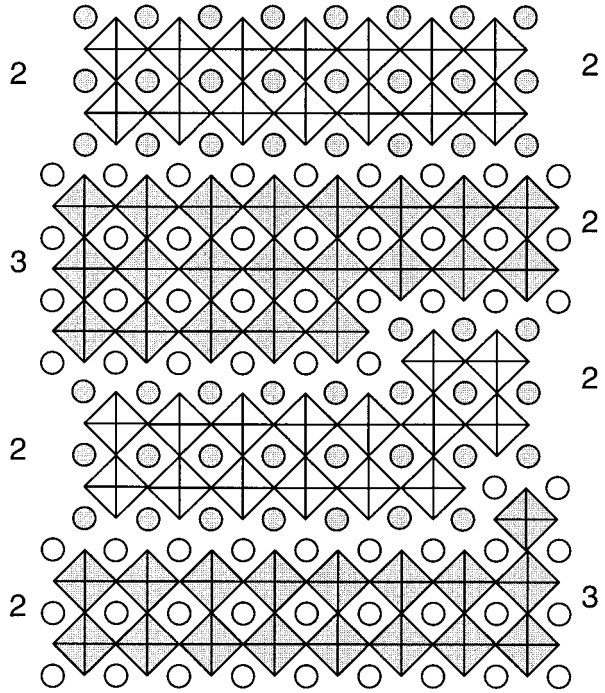

Figure 7. (a) Schematic for the nature of defects that decrease the crystallinity in the *ab* plane. The shading indicate the level of the atoms or octahedra. The value of m adopted locally is shown.

(21) Press, W. H.; Teukolsky, S. A.; Vellerling W. T.; Flannery, B. P. *Numerical Recipes: The Art of Scientific Computing,* 2nd ed.; Cambridge University Press: Cambridge, 1992.

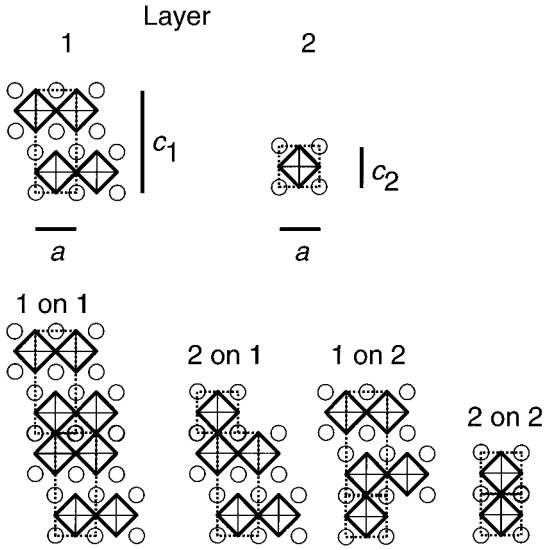

Figure 8. Schematic figure of the cells that comprise the layers used in the DIFFAX simulation and the various modes of stacking.

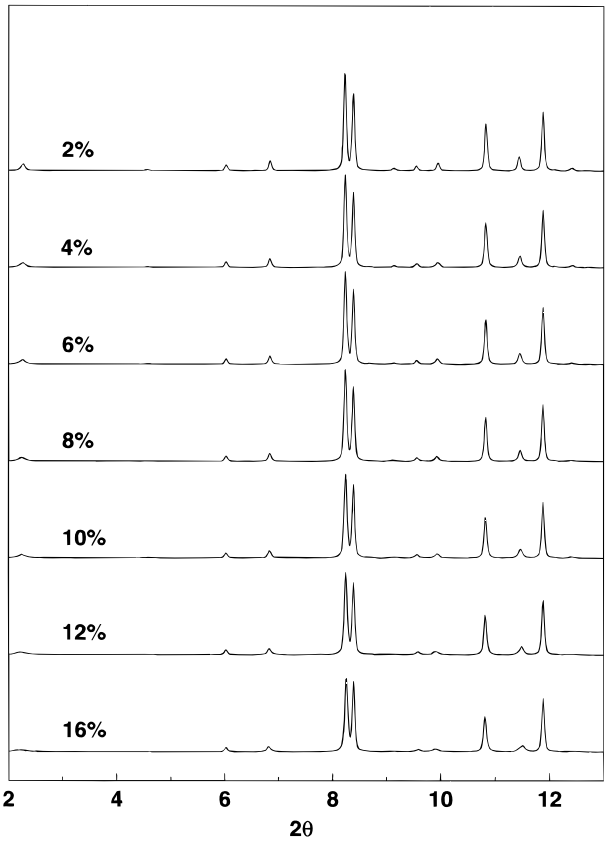

Figure 9. Diffraction patterns simulated using the DIFFAX program in the manner mentioned in the text. The probabilities of the intergrowth defects are marked in the figure.

Figure 9 shows the evolution of the simulated patterns with probability p that the stacking of the double perovskite layers is interrupted by an additional perovskite layer. The Monte Carlo method was used to generate the stacking sequences for these simulated patterns. With an increase in p, there is a clear change in the intensities and widths of some peaks, particularly the two strongest peaks (whose intensities are switched) and the 00*l* reflections which broaden. From visual

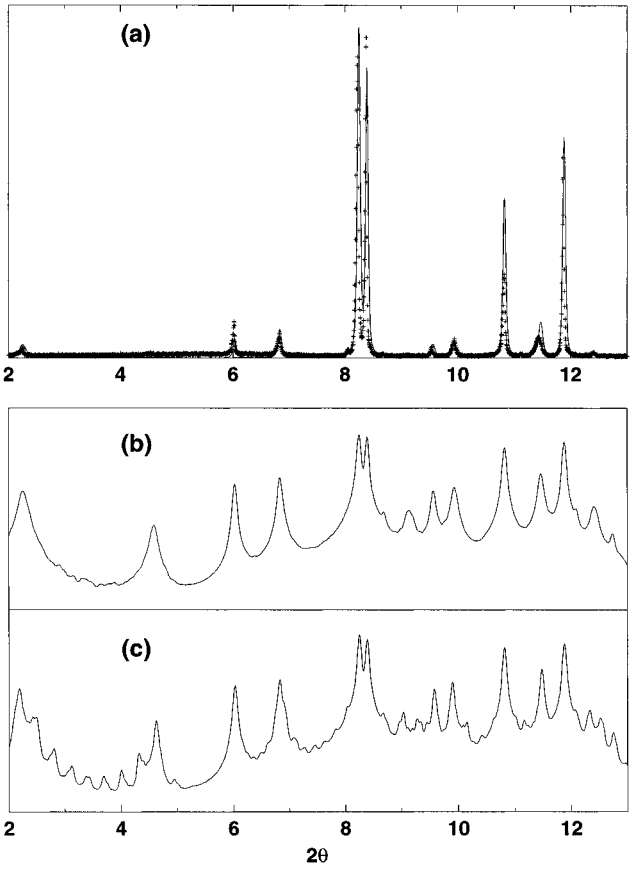

Figure 10. (a) Comparison of the experimental SXPD pattern (points) and the pattern simulated using DIFFAX for a defect probability of $p = 10\%$. (b) A comparison of the DIFFAX simulation using a random sequence (Monte Carlo) and (c) the Sobol′ sequence to generate the stacking. The latter corresponds to staging of the defects and shows more structure. For these simulations $p = 10\%$. The counts in (b) and (c) are shown on a log scale.

comparison it was clear that the experimental SXPD pattern was close to the $p = 10\%$ defect model. While the intensities of the two main peaks are still not properly captured, exceeding this value of p results in very broad 00*l* peaks and an almost vanishing intensity for the 002 peak. The considerable computational effort involved in the DIFFAX calculation precludes the *refinement* of the defect probability p or any other parameter. In panel (a) of Figure 10, we present the experimental pattern and the $p = 10\%$ DIFFAX simulation. Considering the simplicity of the model, the correspondence is remarkable and allows us to estimate that on average, an extra perovskite layer is inserted into the structure after every 10 or so double perovskite layers. Panel (b) of this figure compares the simulated patterns without staging (using Monte Carlo) and with (using Sobol′). There is clearly some structure to the peaks in the latter case, due to the formation of superstructures. The absence of such structure in the SXPD patterns suggests that staging of the intergrowth defects is not a phenomenon observed in the present system. This is broadly in keeping with the HREM images. Also in keeping with the HREM images, we attempted to cluster the faults using sequences which were partly perfectly crystalline and partly fault-ridden. This did not improve the fit to the data, although the number of parameters describing the faulting (fault probability p and length of the purely crystalline stacks) was now doubled.

(22) Safran, S. A. In *Solid State Physics*; Ehrenreich, H., Turnbull, D., Eds.; Academic Press: New York, 1987; Vol. 40.

While our modeling of the defect structure is plausible, involving the intermittent insertion of extra perovskite layers into an otherwise perfect $m = 2$ Ruddlesden−Popper phase, its accuracy is in some question since the HREM images suggest large, mostly defect-free crystals, occasionally punctuated by domains with high defect densities.

Structure Refinement. X-ray diffraction data were collected at four wavelengths; one far from the La K edge (∼0.4 Å) and three near the edge in the vicinity of 0.318 Å. The actual values of the wavelengths were refined using a Si standard initially and then the title phase as a secondary standard. Rietveld refinements of the data were carried out using the XND program.[23] The starting parameters were taken from the earlier work using laboratory X-ray data.[9,14] As we have done previously, we coupled the occupancies of La and Sr between the P and R sites in a manner that conserved the crystallographic occupancy of the two sites and the correct stoichiometry of the cations. The refinement of the off-edge data collected with a wavelength of ∼0.4 Å was straightforward, except that the very high resolution of the diffractometer revealed strong line broadening of the 00*l* reflections (which is important for the DIFFAX simulation). To deal with this, Gaussian and Lorentzian components for the line widths for each of three different orientations; along [001], [100], and [110] were introduced. To reduce correlation, these various widths were refined in alternate cycles.

The treatment of the anomalous scattering has been presented in more detail elsewhere.[24] Figure 11 shows the experimental points and the refined profile for the 0.4 Å data. The calculation from which the refined profile was obtained in this figure actually involved the refinement of a single structural model against three SXPD data, one off-edge and two anomalous. In Table 1 we present the results of a refinement of the crystal structure of $La_{1.2}Sr_{1.8}Mn_2O_7$ using three wavelengths. The structure obtained from the present refinement matches that obtained from the refinement of laboratory X-ray data but is of greater precision. It lends credence to our previous conclusions on the effect of (RE,Sr) size and of Mn oxidation state on the manner in which rare-earth and Sr atoms distribute between the P and R sites:[9,14] In this structure (Table 1) it is very clearly seen that the La and Sr ions are *not* distributed over the P and R sites in a random manner.

Magnetism and Magnetotransport. While the transport and magnetic properties of these $m = 2$ manganites have been studied since the early work of McChesney[1] and Rao[2] and their co-workers and more recently in light of their GMR properties,[7−9,25−27] we felt it was of interest to examine closely the properties of a sample whose microstructure was well characterized.

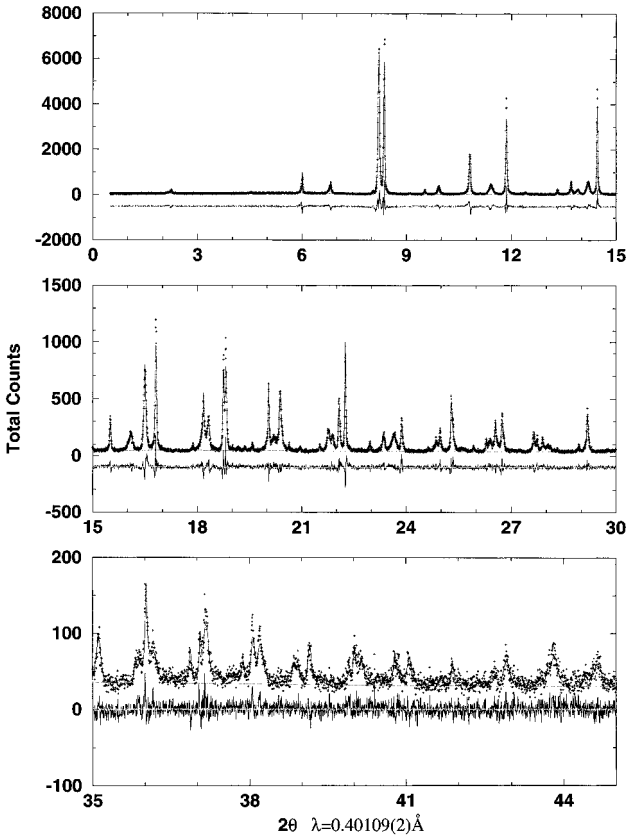

Figure 11. Experimental and refined synchrotron X-ray diffraction powder diffraction pattern of the title phase. The wavelength is indicated. The difference profiles have been offset for clarity.

The results of the defect simulation using the SXPD data combined with the extensive microscopy has allowed estimates of the nature and quantity of defects to be proposed. We thus interpret the magnetotransport within a framework that safely ignores the role of intergrowth defects, since we know their proportion is small. More importantly, there are very few defects in the *ab* plane. Figure 12 shows the results of a susceptibility study on the title phase at high and intermediate temperatures using a Faraday balance. The sample was heated and cooled in a low pressure of He as an exchange gas. The susceptibility was measured on heating the sample. A field of 0.3 T used for the measurement was turned on before every measurement. The value at ambient temperature was acquired once again at the end of the experiment in order to verify the integrity of the sample. From the plot of $1/\chi$ vs T shown in Figure 12, it is seen that deviation from Curie−Weiss behavior commences at temperatures as high as 500 K. A fit above this temperature to the data using the parameters indicated in the figure yields a temperature intercept of 292 K, suggesting strong ferromagnetic interaction. The slope yields $\mu_{eff} = 4.8$ μ_B which is enhanced from the expected value of 4.5 μ_B. Such enhancement has been observed in other manganites.[28]

Figure 13 shows the results of a SQUID study. To avoid effects of hysteresis, the magnetization as a function of temperature for different fields was acquired over five independent runs, after cooling under zero

(23) Bérar, J. F.; Garnier, P. *Accuracy in Powder Diffraction;* Proc. II Intl. Conf., Gaithersburg, 1992 and *NIST Special Publ.* **1992,** *846,* 212. The program and documentation are available by anonymous ftp from rx-crg1.polycnrs-gre.fr.

(24) Seshadri, R.; Martin, C. *European Synchrotron Radiation Facility User Report Ch195-1996.*

(25) Battle, P. D.; Green, M. A.; Laskey, N. S.; Millburn, J. E.; Rosseinsky, M. J.; Sullivan, S. P.; Vente, J. F. *J. Chem. Soc., Chem. Commun.* **1996,** 767.

(26) Battle, P. D.; Blundell, S. J.; Green, M. A.; Hayes, W.; Honold, H.; Klehe, A. K.; Laskey, N. S.; Millburn, J. E.; Murphy, L.; Rosseinsky, M. J.; Samarin, N. A.; Singleton, J.; Sluchanko, N. E.; Sullivan, S. P.; Vente, J. F. *J. Phys. Condensed Matter* **1996**, *8*, L427.

(27) Asano, H.; Hayakawa, J.; Matsui, M. *Appl. Phys. Lett.* **1996**, *68*, 3638.

(28) Brítico, J.; Alascio, B.; Allub, R.; Butera, A.; Caneiro, A.; Causa, M. T.; Tovar, A. *Phys. Rev. B* **1996**, *53*, 14020.

Table 1. $La_{1.2}Sr_{1.8}Mn_2O_7$ Crystal Structure from Rietveld Refinement of Synchrotron X-ray Data

space group: *I*4/*mmm* (No. 139)
temperature: 291 K
wavelengths used: $\lambda_0 = 0.401\ 09(2)$ Å, $\lambda_1 = 0.318\ 37(2)$ Å, $\lambda_2 = 0.318\ 48(2)$ Å
lattice parameters: $a = 3.87337(8)$ Å, $c = 20.1080(8)$ Å
reliability factors:[a] $R_{wp} = 15.1\%$, $R_I = 6.23\%$, $wR_I = 5.67\%$, $wR_F = 2.87\%$

atom	site	*x*	*y*	*z*	*B*(equiv) (Å²)	rel amount[b]	$B_{11} = B_{12}$ (Å²)	B_{33} (Å²)
La(P)	2b	0	0	1/2	0.48	1.02(1)	0.43(4)	0.15(2)
Sr(P)	2b	0	0	1/2	0.48	0.98(1)	0 43(4)	0.15(2)
La(R)	4e	0	0	0.31710(4)	0.50	1.38(1)	0.47(2)	0.13(1)
Sr(R)	4e	0	0	0.31710(4)	0.50	2.62(1)	0.47(2)	0.13(1)
Mn	4e	0	0	0.0972(1)	0.12		−0.06(1)	0.12(2)
O1	2a	0	0	0	1.8(2)			
O2	8g	0	1/2	0.0950(2)	0.38(6)			
O3	4e	0	0	0.1954(4)	1 1(1)]			

Mn−O(1): 1.955(2) Å
Mn−O(2): 1.9372(2) Å
Mn−O(3): 1.973(6) Å
Mn−O(2)−Mn: 177.33(2)° Å

[a] wp = weighted profile, *I* = intensity, $F = \sqrt{I}$. [b] In number of atoms per unit cell.

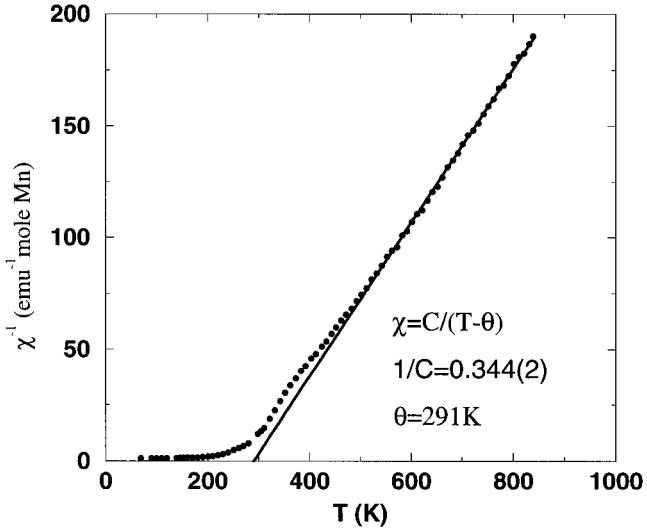

Figure 12. Inverse susceptibility as a function of temperature for the title phase acquired under a 0.3 T field. The fitted line uses the parameters indicated.

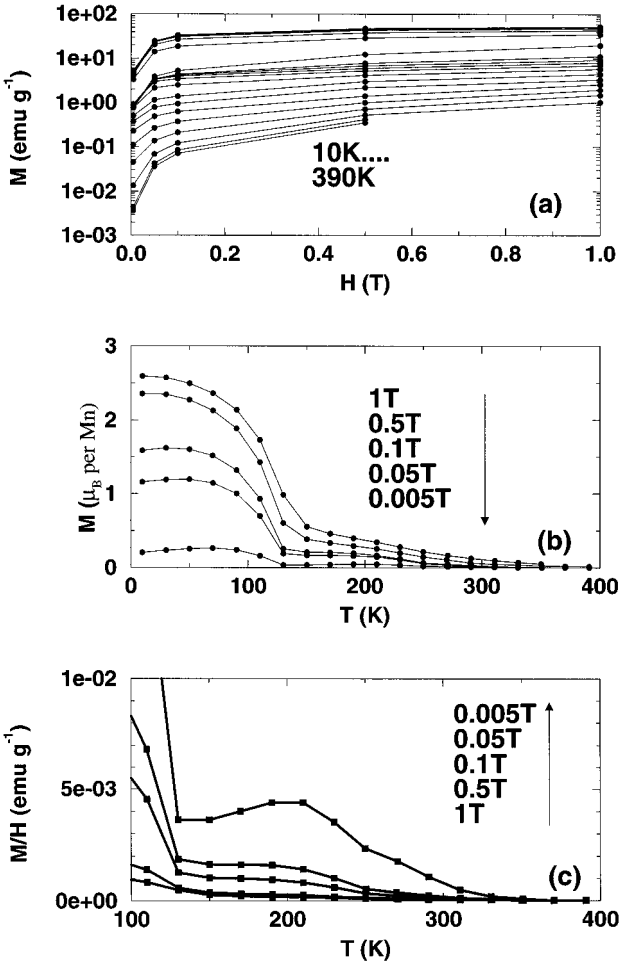

Figure 13. (a) Magnetization as a function of field for the title phase acquired at different temperatures. (b) Magnetization as a function of temperature for data acquired under different temperatures. (c) Susceptibility *M*/*H* of the title phase as a function of temperature.

field. Figure 13a shows the magnetization of the title phases as a function of magnetic field at temperature intervals of 20 K between 10 and 390 K. Even at temperatures as high as 390 K the sample shows nonlinear *M*−*H* curves indicating some sort of magnetic ordering, in support of the Faraday balance data. In Figure 13b, the temperature dependence of the SQUID magnetization under the different fields is shown. Below 130 K there is a transition to bulk ferromagnetism as reported. The transition temperature is independent of field and unambiguously fixed to be between 130 and 110 K from Arrot plots of M^2 vs H/M, which show a change of slope between these temperatures. In this figure, we have reported the magnetization in bohr magnetons to facilitate comparison with the expected saturation value of 3.6 per Mn atom. The feature that we note particularly in Figure 13b is the field-dependent transition that sets in at higher temperatures, seen as an enhancement of the magnetization. A plot of *M*/*H* vs *T* over a smaller temperature regime is shown in Figure 13c, allowing this transition to be seen more clearly. Note the difference in the field dependence of the susceptibility, *M*/*H*, which is suppressed by the application of a magnetic field as seen in Figure 13c when compared with the magnetization which is enhanced (Figure 13b) by the field. This finite magnetization has been remarked by Moritomo[7] as arising from the presence of ferromagnetic correlations over a local scale within the double perovskite block of the title phases; their studies on single crystals suggest that the easy axis of magnetization is in the plane and that the magnetization is strongly anisotropic. The field dependence suggests a similarity to the Kosterlitz−Thouless[29] transition seen in 2D *XY* ferromagnets such as A_2CuF_4,[30] although there could be a finite component of the magnetic moment along $\vec{c}$. The transition at 130

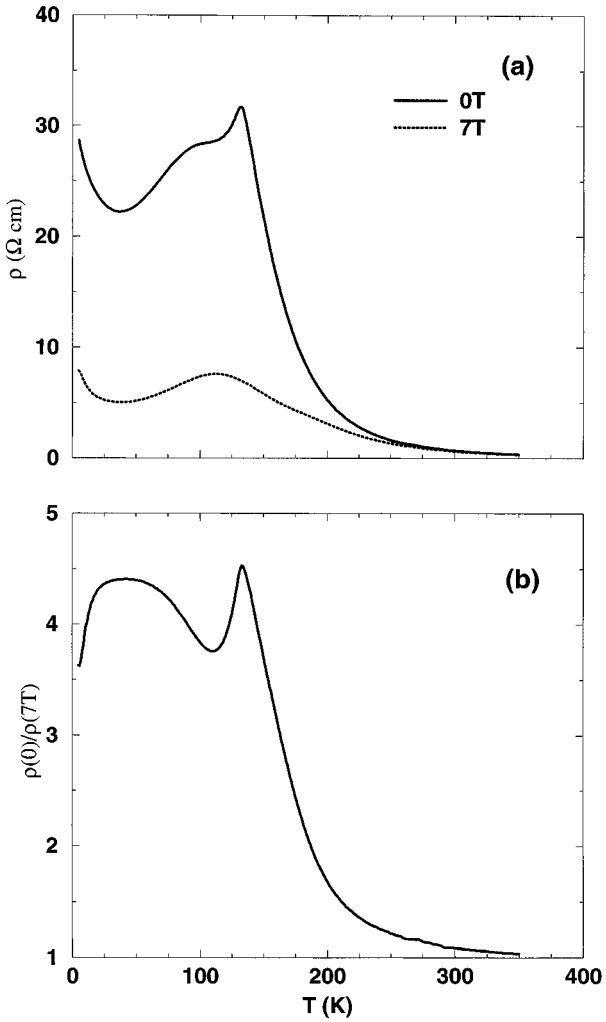

Figure 14. (a) Resistivity as a function of temperature for the title phase under fields of 0 and 7 T. (b) Magnetoresistance ratio $\rho(0)/\rho(T)$ as a function of temperature.

K then corresponds to bulk ferromagnetism setting in with the individual double perovskite layers also coupling ferromagnetically. The possibility of the high temperature transition at ~500 K arising from superparamagnetism has been ruled out by considering plots of M as a function of H/T. For a superparamagnet, such plots would collapse on to a single curve and this is not observed.

The high temperature transition to a phase with local ferromagnetic correlations affects the magnetotransport in these phases. In Figure 14a we show the temperature dependence of the resistivity of the title phase in the absence and under a 7 T magnetic field. The simultaneous onset of bulk ferromagnetism with a change in the sign of the temperature coefficient of resistance (signifying metallic behavior) in this system has been well documented. More recently, the large decrease in the resistivity on the application of a magnetic field has received attention. This is demonstrated here by the application of a 7 T magnetic field. In these and the related perovskite manganites, electron transport takes place with spin memory.[5,6] The scattering of charge carriers is therefore much less effective in the ferromagnetic phases giving rise to the ferromagnetism being accompanied by metallic behavior, or at least a decrease in the electrical resistivity. An examination of many of the perovskite manganites which show GMR properties reveal that the application of a magnetic field results in no change in the activation energy obtained from the $\rho-T$ curves far above the ferromagnetic transition. This is in contrast to the title phase. Here we observe the onset of negative magnetoresistance properties well above the temperature where bulk ferromagnetism sets in, though the onset of bulk ferromagnetism near 130 K does result in a peak in the ratio $\rho(0)/\rho(7\ \mathrm{T})$ shown in Figure 14b. The key point is that GMR does not depend on the existence of bulk ferromagnetism and local ferromagnetic correlations are sufficient for GMR to manifest itself. This has been amply demonstrated in small particles of perovskite manganites which display GMR in the absence of bulk ferromagnetic ordering.[31]

Another feature of note in the electrical transport in these systems is the broad transition at low temperatures both under and in the absence of a field that returns the system to insulating behavior. This is seen in many of the perovskite manganites and testifies to the importance of disorder in these oxides which intrinsically have site randomness. However, we note as we have in an earlier publication on a related system,[32] that the localization is much more dramatic in these quasi-2D systems, with a larger rise in the resistivity. This is broadly in keeping with the scaling theory of localization which suggests that in 2D and at large enough length scales, only localized behavior is possible.[33] A striking parallel is in the layered high-T_C cuprates which as a function of doping, change from superconducting to insulating with no intermediate metallic phase being exhibited.[34]

Acknowledgment. We thank Gavin Vaughan of the ESRF for help with data collection and Marie France Rondeau for the oxygen analysis. This work was supported by the European Community, contract CI*-CT94-0107.

CM9605936

(29) Strandburg, K. J. *Rev. Mod. Phys.* **1988**, *60*, 161.
(30) (a) Dekker, C.; Arts, A. F. M.; deWijn, H. W. *Phys. Rev. B* **1988**, *38*, 11512. (b) Hirakawa, K.; Ubukoshi, K. *J. Phys. Soc. Jpn.* **1981**, *50*, 1909.
(31) Mahesh, R.; Mahendiran, R.; Rao, C. N. R. *Appl. Phys. Lett.* **1996**, *68*, 2291.
(32) Seshadri, R.; Maignan, A.; Hervieu, M.; Nguyen, N.; Raveau, B. *Solid State Commun.* **1997**, *101*, 453.
(33) Lee, P. A.; Ramakrishnan, T. V. *Rev. Mod. Phys.* **1985**, *57*, 287.
(34) Iye, Y. In *Metal-Insulator Transitions Revisited*; Edwards, P. P., Rao, C. N. R., Eds.; Taylor and Francis: London, 1995.